Nanoscale

PAPER

View Article Online
View Journal | View Issue

Cite this: *Nanoscale*, 2023, **15**, 5469

Metal oxide cluster-assisted assembly of anisotropic cellulose nanocrystal aerogels for balanced mechanical and thermal insulation properties†

Huihui Wang,[a,d] Bingyu Xia,[b] Rui Song,[b] Wei Huang,[d] Mingxin Zhang,[d] Chuanfu Liu,*[b] Yubin Ke,[c] Jia-Fu Yin,*[a,c] Kun Chen *[a] and Panchao Yin *[a,c]

Cellulose nanocrystal (CNC) materials grant abundant possibilities for insulation, however, their extensive application is hindered by the intrinsic tradeoff between their thermal insulating performance and mechanical properties. Here, we show that CNC aerogels with balanced thermal and mechanical performance can be fabricated *via* a 1 nm metal oxide cluster (phosphotungstic acid, PTA)-assisted unidirectional freeze-drying processing. The as-prepared hybrid aerogels with hierarchical porous structures consisting of layer-by-layer CNC nanosheets enable the decoupling of the strengthening of mechanical properties and the enhancement of thermal insulating capabilities. Within layered structures, the surface-doped nanosized PTA clusters with negative charges behave as dynamic physical cross-linking points, and continuous networks of PTA-doped CNC can be formed *via* multiple supramolecular interactions (*e.g.*, electrostatic attractions and hydrogen bonds). The afforded stable three-dimensional network structures are able to withstand externally applied forces and large deformations, endowing the aerogels with excellent mechanical performance. Moreover, the inter-layer gap is dominated by nanopores, endowing much lower thermal conductivities along the radial direction in comparison to the axial direction. The addition of PTA clusters also contributes to the obvious enhancements of the fire-retardant properties. Our discoveries provide a facile approach for the design and scalable production of CNC-based insulation materials with optimized mechanical properties and additional fire-retardant properties.

Received 23rd November 2022,
Accepted 14th February 2023

DOI: 10.1039/d2nr06551g

rsc.li/nanoscale

Introduction

The unending reliance on fossil fuels has produced excessive CO_2 emissions that undoubtedly brings severe damage and pollution to our environment.[1] Owing to the unsatisfactory thermal insulating performance of currently available insulation materials, massive energy is needed to maintain a comfortable indoor temperature for the building environment,[2] accounting for over 10% of the total global energy consumption. Therefore, insulating materials with lower thermal conductivity are urgently required to mitigate severe global climate change.[3,4] Aerogels, bearing abundant porosity and high air volume of (~85%) have been broadly exploited as high-performance thermal insulating materials for thermal control systems in buildings and spacecrafts.[5–7] As for the thermal transport mechanism, solid conduction, gas conduction, and thermal radiation cooperatively contribute to the total thermal conductivity of aerogels.[7,8] The highly porous microstructures accompanied by distorted continuous networks are not favorable for phonon conduction through the solid pathway.[9] Moreover, the intrinsic abundant pore walls facilitate heat reflection and refraction, greatly suppressing the thermal radiation effects.[10] The heat transport from gas is usually regarded as the predominant thermal contribution in aerogels.[11] When the pore dimension is below the mean free path of air molecules (50 nm, at room temperature and atmospheric pressure), thermal conduction resulting from the collision of the air molecules could be significantly reduced.[12–15] Nowadays, highly developed molecular engineering provides a powerful toolbox for

[a]*South China Advanced Institute for Soft Matter Science and Technology, State Key Laboratory of Luminescent Materials and Devices, South China University of Technology, Guangzhou, 510640, China. E-mail: yinpc@scut.edu.cn, mschenk@scut.edu.cn, yinjf@scut.edu.cn*
[b]*State Key Laboratory of Pulp and Paper Engineering, South China University of Technology, Guangzhou, 510640, China*
[c]*Guangdong-Hong Kong-Macao Joint Laboratory for Neutron Scattering Science and Technology, Dongguan, 523803, China*
[d]*State Key Laboratory of Marine Resource Utilization in South China Sea College of Materials Science and Engineering, Hainan University, Haikou 570228, P. R. China*
† Electronic supplementary information (ESI) available. See DOI: https://doi.org/10.1039/d2nr06551g

the design of versatile aerogels with customized dimensions and well-controlled interfaces.

Cellulose nanocrystals (CNCs), mainly extracted from wood and other biomass, are typical renewable biopolymers with abundant resources,[16,17] which provide new possibilities for the construction of thermal insulating materials from supramolecular nanoscale engineering.[18–20] It has been reported that weak interactions (*e.g.*, hydrogen bonds and van der Waals interaction) are unfavorable for phonon propagations,[21,22] contributing to the improvement of the thermal insulation performance of CNC aerogels.[5] However, this type of aerogels usually suffers from poor mechanical properties because of their weak inter-connected structural units and resultant unstable skeletons.[23] Traditional approaches for mechanical property enhancement are mainly associated with the reinforcement of aerogels' network density and integrity *via* strong attractions.[24–26] Nevertheless, the remarkably increased network density in turn benefits phonon propagation, thus increasing its thermal conductivity.[27] Meanwhile, the flammability of CNC-derived aerogels hinders their extensive applications.[18] When facing extreme fire injury conditions, the CNC-derived aerogels with poor fire-retardant performances will easily be burned out. Therefore, it remains a great challenge for the construction of CNC aerogels with balanced thermal insulation ability, fire-retardant performance, and mechanical properties. In this work, CNCs are utilized as green building blocks for preparing aerogels. We successfully fabricate porous anisotropic long-range lamellar structured CNC aerogels by phosphotungstic acids ($H_3[P(W_3O_{10})_4]\cdot nH_2O$, denoted as PTAs)-assisted unidirectional freeze-drying. The as-formed lamellar assemblies are dynamically joined by the PTA clusters to form 3D network structures *via* supramolecular complexation. The large scaled anisotropic structures account for the high mechanical strength, while the dynamic cross-linking networks promote aerogels' flexibility and elasticity. Hence, the optimized network structures grant the composite aerogels with observable excellent mechanical properties. Meanwhile, the aerogels' pore dimensions and hierarchical structures can be effectively regulated by physically depositing the PTA clusters or chemically grafting the amino-silane groups on the surfaces of CNC, followed by governing the materials' thermal insulation performance. More importantly, the inorganic nanofiller (PTA cluster) incorporation is found to profoundly enhance the fire-retardant ability, which indeed promotes the composite aerogels' extensive applications.

Experimental section

Materials

CNC suspension, PTA clusters, and 3-aminopropyltrimethoxysilane (APTS, 97%) were purchased from commercial sources and used without further purification.

Preparation of CNC aerogel. The CNC suspension was diluted to 3.0 wt%, and the diluted CNC suspension with a gel state is denoted as the CNC hydrogel. Then, the CNC hydrogel was unidirectionally frozen and dried in a freeze dryer (FM25XL-70, SP Scientific, UK) to obtain the CNC aerogel.

Preparation of CNC/PTA aerogel. 20 mg of PTA was directly added into 3 wt% of CNC suspension (20 g). The mixture was stirred at room temperature for 30 min and the formed gel-state sample was denoted as the CNC/PTA hydrogel. The CNC/PTA hydrogels were subsequently treated in a homemade unidirectionally freezing instrument to induce the directional alignments of CNCs rods. After that, the frozen CNC/PTA hydrogel was transferred into a freeze dryer (FM25XL-70, SP Scientific, UK) for 48 h to remove the solvents and then to obtain the highly anisotropic CNC/PTA aerogel.

Preparation of A-CNC aerogel. The surface of CNC was modified with APTS. Specifically, APTS at a liquid ratio of 1% was added dropwise into the 3 wt% of CNC suspension (10 g) with a magnetic stirrer at room temperature for 4 h. After the modification, the formed gel-state A-CNC suspension was named A-CNC hydrogel. A-CNC hydrogels were directionally frozen with liquid nitrogen and then sublimated to obtain A-CNC aerogel.

Preparation of A-CNC/PTA aerogel. PTA clusters (20 mg) were directly added to the A-CNC suspension. The mixture was stirred for 30 min at room temperature and named A-CNC/PTA hydrogel. Then, A-CNC/PTA hydrogels were subsequently treated for unidirectional freeze-drying in a liquid nitrogen bath. The solvent was sublimated and removed to obtain the A-CNC/PTA aerogel.

Characterization

The chemical structures of CNC, PTA, and the prepared aerogels were characterized using an FT-IR spectrometer (Nicolette IS50-Nicolet Continuum, US), and the spectra were recorded in the range of 4000–400 cm^{-1}. The microstructures of aerogels were studied using a scanning electron microscope (SEM, ZEISS G300, Germany). The morphology of the CNC with different surface structures was characterized using an atomic force microscope (AFM, Bruker MultiMode 8, Germany). Small-angle X-ray scattering (SAXS) data were collected at the beamline (BL-16B and BL-19U) of the Shanghai Synchrotron Radiation Facility (SSRF) with a Pilatus 2M detector. The scattering vector q was calculated to be $q = 4\pi(\sin\theta)/\lambda$, in which 2θ is the scattering angle. The exposure time is set as 100 s for aqueous samples and 10 s for solid samples. Software Raw was used to process the SAXS data and the background scattering was subtracted. Small angle neutron scattering (SANS) experiments were carried out at the China Spallation Neutron Source (CSNS) platform. The N_2 adsorption data of the aerogel samples at −196 °C was recorded on an analyzer (ASAP 2460, Micromeritics, Shanghai, China). The specific surface area and pore dimension information were obtained from the Brunauer–Emmett–Teller (BET) analytical methodology. The elemental analysis of samples (3–5 mg) was studied using the Elementar Vario EL cube (Germany) instrument.

Thermal conductivity test. The thermal conductivity tests on CNC aerogels were performed on a Hot Disk TPS 2500 S instru-

ment (Hot Disk AB, Sweden), and the thermographic images were recorded using an infrared thermal camera (TiS40, Fluke Co., Ltd, USA). During the measurements, the ambient temperature was kept at around 30 °C.

Flame self-extinguishing tests. The CNC aerogels were ignited for 1 s by an alcohol blow torch. A timer was used to calculate the flame self-extinguishing time. The burning process of the CNC aerogel was also recorded using a digital camera. The analysis of the combustion behaviour of the aerogels was carried out with a cone calorimeter device (Fire Testing Technology, FTT, UK) according to ISO5600 under a heat flux of 35 kW m^{-2}.

Mechanical tests. The compression data of aerogels (35 × 25 × 10 mm) were recorded on a compression machine Instron 5565 (US). The maximal compression strain was set as 50%, and the compression tests were recycled 100 times with a compression rate of 10 mm min^{-1}.

Results and discussion

Structural characterizations of the hydrogels and the corresponding aerogels

The unidirectional freezing methodology provides a facile approach to afford highly oriented lamellar structures.[28,29] The detailed preparation information of the hydrogels during the unidirectional freezing is summarized in the Materials and methods section (Fig. S1†). A mechanical rheometer was used to assess the viscoelastic performances of the as-prepared hydrogels. As shown in Fig. S2,† all the hydrogels delivered a predominant elastic response to the applied deformations, evidenced by the higher storage modulus (G') than loss modulus (G'') in the testing frequency range.[30] Moreover, the shear moduli for CNC/PTA and A-CNC/PTA hydrogels were much higher than the corresponding un-doped CNC and A-CNC counterparts. The rational explanation is that a part of the nanosized PTA clusters inside the hydrogel behaves as physical cross-linking points, which promotes the generation of more stable network structures with much higher cross-linking densities.[31] Consequently, the afforded CNC/PTA and A-CNC/PTA hydrogels are more robust with higher apparent mechanical strength.

The microscopic structures of the hydrogel samples were assessed by SAXS methodology.[32] Judging from the experimental SAXS curves, no sharp crystallized peaks were detected in the whole q ranges (Fig. 1a). This indicated a homogenous distribution of the nanoscaled PTA clusters inside the gel skeletons due to strong attractions among the CNC rods and PTA units.[33] As a way to extract a more structure information about the gels, typical Lorentzian models (Fig. S3, ESI†) were exploited to fit the experimental SAXS data. The correlation lengths (ξ), associated with the average mesh sizes for the gel networks can be directly accessible from the data fitting process, which is summarized in Fig. 1b. The correlation length value of A-CNC/PTA hydrogel is obviously larger than that of A-CNC hydrogel, originating from the electrostatic

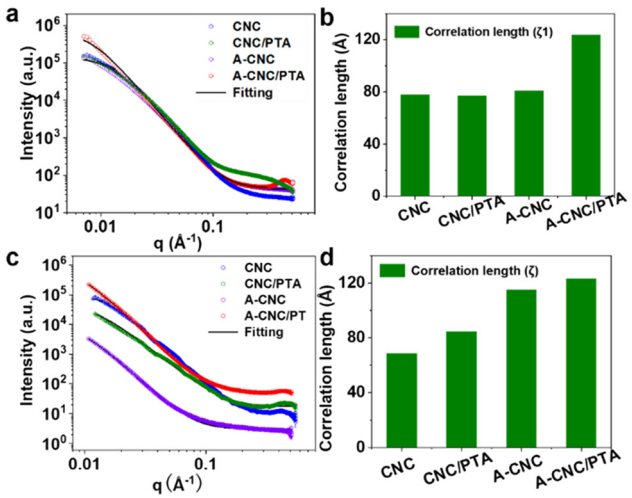

Fig. 1 (a) SAXS data and (b) fitted correlation lengths of the CNC hydrogels. (c) SAXS data and (d) fitted correlation lengths of the CNC aerogels. The fitting profile based on the Lorentzian model is shown as black solid lines in Fig. 1a and c.

repulsion effects between the deposited anionic PTA clusters. However, no change in the correlation length was observed after the introduction of PTA units into the CNC gels (Table S3†). As is well-known, neutron mainly interacts with the atomic nucleus, which is ultimately different from the interaction mode of X-ray. SANS techniques show high sensitivities toward light elements, especially hydrogen, and their isotopes.[34] Therefore, the SANS data indeed reflect the spatial distribution information of CNC rods in the gel networks. The correlation lengths afforded from the Lorentzian fitting of the SANS data are close to that obtained from the SAXS data analysis (Fig. S4†). The self-consistent of correlation length in PTA-incorporated hybrid gels from different scattering tests unambiguously demonstrates that the PTA clusters are deposited onto the surfaces of CNCs.[33]

Unidirectional freezing, also named freeze-casting, was applied to produce anisotropic CNC and its composite aerogels. During the unidirectional freezing process, the ice crystals gradually grow due to the imposed temperature gradient, which provides confined environments at nanometer scales to drive the alignment of CNCs along a specific direction.[29] After removing the solvents under freeze-drying conditions, the porous microstructures were maintained to the maximum extent (Fig. S5†). The SAXS method was further exploited to unveil the hierarchical structures of the resultant aerogels. Similar to the hydrogel samples, the incorporated PTA clusters remained homogeneously distributed in all the aerogels, as suggested by the SAXS curves (Fig. 1c). The obtained SAXS data were all well-fitted by the same Lorentzian function, which subsequently produces the correlation length parameters (Fig. 1d). By comparison, the correlation length slightly decreases from 7.8 nm (CNC hydrogel) to 6.9 nm (CNC aerogel), which is due to the partial collapse of the CNC network resulting from the capillary effect during the freeze-

drying process (Table S4†).[35] The average correlation lengths of CNC/PTA, A-CNC, and A-CNC/PTA aerogels are 8.5, 11.5, and 12.3 nm, respectively, which are higher than that of the CNC aerogel (6.9 nm). This emphasizes that surface-doped PTA clusters or amino-silanized groups can effectively prevent the shrinkage of the gel network during the freeze-drying process (Scheme 1). The average correlation lengths of CNC/PTA, A-CNC, and A-CNC/PTA before and after the freeze-drying operation were determined to be 7.6 *vs.* 8.5 nm, 8.1 *vs.* 11.5 nm, and 12.3 *vs.* 12.3 nm, respectively, which is not much changed during the drying process. Bearing these in mind, a conclusion can be drawn that the surface physical/chemical modifications provide a facile and effective approach capable of weakening the capillary effect to prevent the shrinkage of the gel networks to afford highly porous structures.

During the freeze-drying process, the solvent components of gels are gradually replaced by gas, and the afforded highly porous foam-like aerogels usually deliver extremely low density.[35] As shown in Fig. 2a, our aerogel samples are able to stand on the flower without causing any damage to the petals, characteristic of their lightweight features (Table S1†). Structural analysis of scanning electron microscopy (SEM) of CNC and PTA/CNC aerogels clearly revealed the large scaled lamellar assemblies aligned towards the selected direction (Fig. 2c). The CNC rods are highly oriented inside the lamellar assemblies due to the imposed nanoconfined environments.[36] When surfaces of CNCs are chemically grafted with amino-silanized groups, the highly directional arrangements of CNC rods are conformationally unfavorable owing to the enhancement of steric effects from the surface-grafted groups and PTA clusters. Therefore, the overall sizes of the as-formed lamellar assemblies accordingly decrease and evident distortions of the lamellar structures can be observed as suggested from the SEM images of A-CNC and A-CNC/PTA aerogels. Energy dispersive X-ray analysis (EDX) clearly shows the enrichment of P and W elements on the lamellar assemblies, confirming the homogenous distribution of the PTA cluster inside the aerogels. The porous properties of the aerogels were evaluated from N_2 adsorption/desorption experiments at −196 °C (Fig. 2b). The

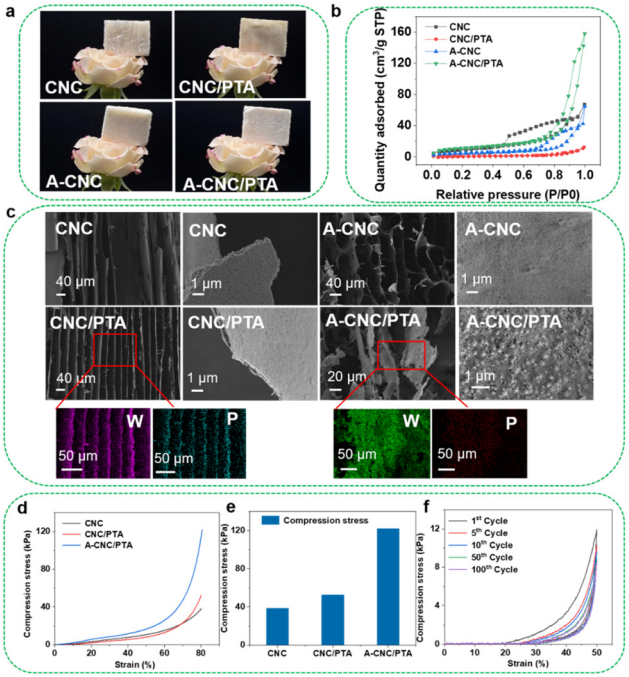

Fig. 2 (a) Photographs of the prepared aerogels. (b) BET adsorption and desorption curves of the aerogels. (c) SEM and mapping images of the aerogels. (d) Compression test curves, (e) compression stress, and (f) cyclic compression tests of the aerogels.

corresponding Brunauer–Emmett–Teller (BET) surface areas (S_{BET}) and the pore dimension information are summarized in Table S2.† By comparing with CNC aerogels (34.3 $m^2\ g^{-1}$), the incorporation of PTA clusters leads to a significant decrease of the S_{BET} of CNC/PTA aerogels (4.9 $m^2\ g^{-1}$) accompanied by the increase in average pore diameter from 8.9 to 23.7 nm. Complexing PTA onto the surface aminosilanated CNCs will not damage the overall porosities of the resultant aerogels, whereas the average pore diameter increases from 8.9 (A-CNC aerogel) to 23.5 nm (A-CNC/PTA aerogel).

The formation of an anisotropic lamellar structure has been reported to cause the enhancement of the mechanical strength,[37–39] which was analyzed from the uniaxial compression test, as shown in Fig. 2d–f. The compressive direction was set to be perpendicular to the alignment direction of CNC rods. The afforded compressive moduli of the aerogel samples delivered a monotonical increase from 139.5 kPa (CNC), 265.2 kPa (CNC/PTA) to 642.2 kPa (A-CNC/PTA) with a maximum compressive strain of 80%. More importantly, the applied deformation onto A-CNC/PTA aerogels can be mostly recovered after the compression loading. The reversible deformation behaviours were further evaluated by the fatigue cyclic compressive tests. Even though the A-CNC/PTA aerogels were compressed 100 times, 40% of the loaded deformation was capable of recovering and the testing specimens were intact without apparent fractures. The comprehensive mechanical properties of A-CNC/PTA aerogels were much improved than those previously reported CNC and their composite aerogels.

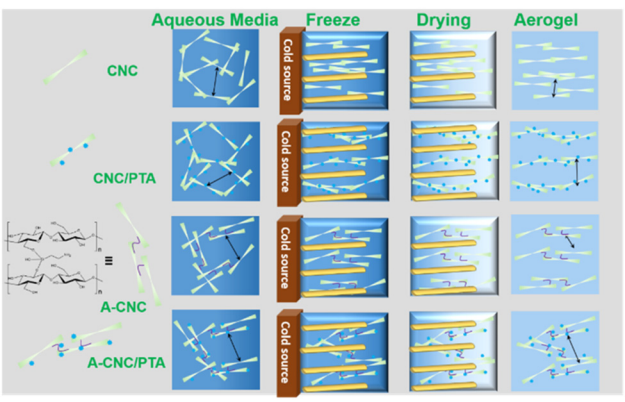

Scheme 1 Formation mechanism of CNC aerogels with different surfaces.

From our point of view, high mechanical strength is mainly correlated with aerogels' anisotropic lamellar structures, while the formation of dynamic cross-linking networks mediated by the PTA clusters indeed contributes to the observed flexibility enhancements.

Thermal insulation performance of CNC aerogels with different surfaces

Due to the existence of thermal convection, conduction, and multiple reflect radiation effects, CNC-based aerogels with the lamellar structure hold great potentials in thermal insulation applications.[3,40] The thermal insulation performances of the CNC, CNC/PTA, and A-CNC/PTA aerogels were further explored. The selected aerogel specimen with specific size (10 × 10 × 10 mm) was placed on the 70 °C hot disk, while the temperature of the aerogel at 0 and 120 min was recorded by the infrared camera. Afterwards, the absolute temperature difference ($|\Delta T|$) determined from the experimental observation can be used to quantitatively evaluate the aerogel's thermal conductivity, which is summarized in Fig. 3b. All the three aerogels (CNC, CNC/PTA, and A-CNC/PTA) presented direction-dependent thermal insulation properties originating from their intrinsic anisotropic microstructures,[3] and their thermal insulation effects in the radial direction were rationally better than those in the axial direction. For the CNC and their composite aerogels, the intrinsic porous networks and abundant pore interfaces inside are not favorable for thermal conduction and radiation. More importantly, the pore dimensions of our aerogels can be effectively regulated to be lower than the mean free path of the air molecules (~50 nm), which profoundly suppresses the heat transport from the gas then to lower down the thermal conductivity of the overall aerogels. Due to the anisotropic structure, the thermal conduction effect from the gas in the radial direction is hugely shielded, providing a rational explanation for the observable directional-dependent thermal conductivity.

Based on the above data, the A-CNC/PTA aerogel showed the lowest thermal conductivity in the radial direction, which was further used to build a nest to evaluate its thermal insulation performance for practical bird egg protection. A quail egg was placed in the aerogel nest, and another one without any protection was set as the control group. The temperature variation of the egg was recorded *via* the infrared image system before or after heating (Fig. 4). As for the control experiment, the egg was roasted at 70 °C for 30 min without any protection, and the detected temperature on the eggshell could reach 56.9 °C, which resulted in the irreversible damages to the egg under testing (Fig. 4e). Instead, the corresponding temperature of the egg protected by the aerogel nest was 12.5 °C lower than that of the control group (Fig. 4f), which demonstrated that the aerogel was capable of protecting the bird egg from heating. After the test, its yolk and white were clearly visible, further confirming the good thermal insulation performance of our aerogels. Bearing these aspects in mind, we believe that the A-CNC/PTA aerogels hold great potential in protecting bird eggs from harsh climatic injuries.

Flame retardancy performance of the CNC aerogels

Fire retardancy properties is urgently demanded in practical thermal insulating materials, especially on facing burning, fire injuries, and other harsh service conditions.[18] However, a non-negligible challenge for biomass-based insulation materials was their poor resistance to fire, which hugely limits their extensive applications. The four afforded aerogel samples (CNC, CNC/PTA, A-CNC, and A-CNC/PTA) were ignited with an alcohol blowtorch, and the combustion processes were recorded using the digital camera, as shown in Fig. 5. The CNC aerogel was highly flammable, and it is quickly burned

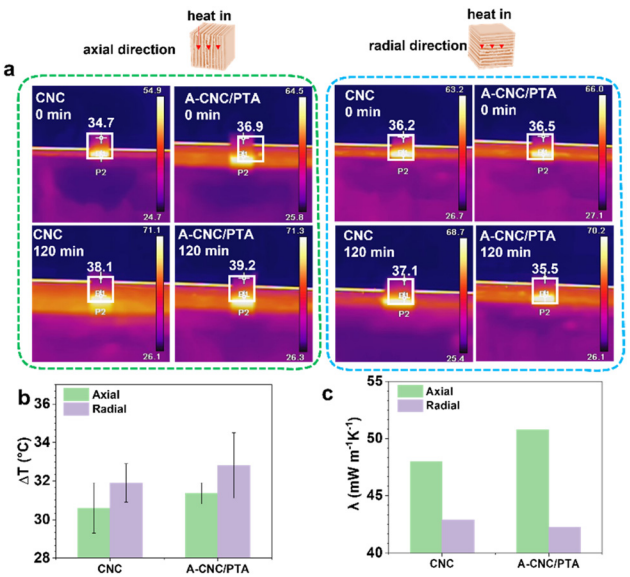

Fig. 3 (a) Infrared images of the aerogels with different surfaces placed on the 70 °C of the hot disk at the axial and radial directions. (b) Temperature differences (ΔT) of the aerogels (10 × 10 × 10 mm) at the axial and radial directions on the 70 °C of the hot disk for 120 min, respectively. (c) Thermal conductivity of the aerogels with different surfaces in the axial and radial direction.

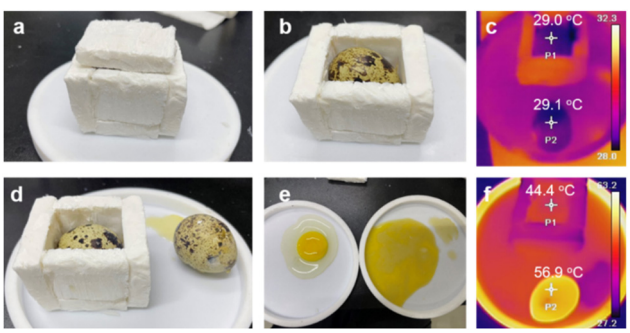

Fig. 4 (a) The customized aerogel nest. (b) One egg was placed in the aerogel nest under thermal protection. (c) Infrared image to show the initial temperature of the two eggs. The appearance (d) and interior biological tissue (e) of the two eggs after the heating treatment. (f) Infrared image to show the temperature of the two eggs during heating.

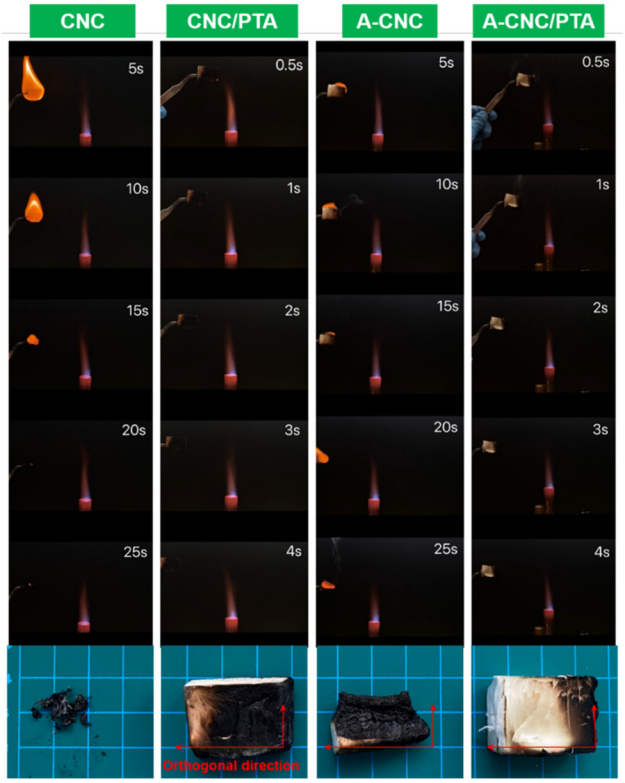

Fig. 5 Fire retardancy experiments of the four aerogels.

out within 15 s. The post modification of silicon-containing groups on the CNC surface leads to improvement of the fire retardancy ability. Therefore, the burning A-CNC aerogel was observed to self-extinguished within 25 s and part of the specimen remained intact after the test. The hybridization of the inorganic nanofillers (*e.g.* metal oxide and nanoparticles) into the aerogels can be considered as an effective strategy to enhance the materials' fire retardancy performance (Fig. S7†).[41] Herein, the fire retardancy ability of the aerogels was significantly promoted after the complexation of PTA with CNCs and their derivatives. The CNC/PTA aerogel exhibited relatively good fire retardancy properties and the burning flame can be quickly self-extinguished within 4 s. Among them, the A-CNC/PTA aerogel presented the best fire retardancy performance (self-extinguished within 1 s), mainly correlated to the synergistic retardancy effects from the surface-doped PTA clusters and aminosilanated groups.[42,43] These could be further demonstrated by the cone calorimetry data (Table S7 and Fig. S8†). The excellent flame retardancy performance of the aerogel A-CNC/PTA grant more opportunities for their practical use on green and highly-efficient thermal insulation building materials.

Conclusions

In summary, a series of CNC and their composited aerogels were facilely fabricated by typical unidirectional freezing methods. The hierarchical anisotropic structures can be effectively regulated by the surface engineering of CNCs (physical and/or chemical modification), which was systematically elucidated by a combination of techniques (*e.g.*, SAXS, SANS, and electron microscopy methodology). The N_2 adsorption experiment revealed the highest specific area of A-CNC/PTA aerogel originating from the surface-grafted PTA clusters and aminosilanization in maintaining the highly porous structures during the freeze-drying process. More importantly, the fatigue cyclic compressive tests clearly revealed the high mechanical strength and excellent flexibility of A-CNC/PTA aerogel, which is superior to most reported CNC-based aerogels. The high specific surface area combined with good mechanical performance make A-CNC/PTA aerogels ideal candidates for thermal insulation applications. Especially, the A-CNC/PTA aerogel presented the typical direction-dependent thermal insulation performance resulting from its' anisotropic microstructures. Moreover, the existence of PTA and amino-silanized groups cooperatively improved the fire retardancy property, contributing to the best performance in fire retardancy experiments for the A-CNC/PTA aerogel. Therefore, the excellent thermal insulation performance and fire extinguishing performance endow the aerogels with great potential for application in green and highly-efficient thermal insulation building materials.

Author contributions

Panchao Yin and Kun Chen conceived the idea and supervised the whole project. Huihui Wang performed the experiments, data analysis, and manuscript preparation. Jia-Fu Yin contributed to data analysis, and manuscript editing. Chuanfu Liu provided financial and technical support. Bingyu Xia, Rui Song, Mingxin Zhang, Wei Huang, and Yubin Ke helped with the data collection. All the authors have read and approved the final manuscript.

Conflicts of interest

There are no conflicts to declare.

Acknowledgements

The authors are grateful for the financial support from the National Nature Science Foundation of China (22101086, 22241501, and 92261117), the Natural Science Foundation of Guangdong Province (2021A1515012024 and 2021A1515010271), and China Postdoctoral Science Foundation (2022M711189, BX20220114).

Notes and references

1 M. Frankignoulle, G. Abril, A. Borges, I. Bourge, C. Canon, B. Delille, E. Libert and J.-M. Théate, *Science*, 1998, **282**, 434–436.

2 Z. Ma, D. Zhao, C. She, Y. Yang and R. Yang, *Mater. Today Phys.*, 2021, **20**, 100465.
3 X. Zhang, X. Zhao, T. Xue, F. Yang, W. Fan and T. Liu, *Chem. Eng. J.*, 2020, **385**, 123963.
4 L. Liu, H. Li, A. Lazzaretto, G. Manente, C. Tong, Q. Liu and N. Li, *Renewable Sustainable Energy Rev.*, 2017, **69**, 912–932.
5 V. Apostolopoulou-Kalkavoura, P. Munier and L. Bergström, *Adv. Mater.*, 2021, **33**, 2001839.
6 U. Berardi, *Energy Build.*, 2018, **159**, 370–381.
7 E. Cuce, P. M. Cuce, C. J. Wood and S. B. Riffat, *Renewable Sustainable Energy Rev.*, 2014, **34**, 273–299.
8 Y.-L. He and T. Xie, *Appl. Therm. Eng.*, 2015, **81**, 28–50.
9 M. Qin, Y. Xu, R. Cao, W. Feng and L. Chen, *Adv. Funct. Mater.*, 2018, **28**, 1805053.
10 K.-Y. Chan, X. Shen, J. Yang, K.-T. Lin, H. Venkatesan, E. Kim, H. Zhang, J.-H. Lee, J. Yu, J. Yang and J.-K. Kim, *Nat. Commun.*, 2022, **13**, 5553.
11 S. Shin, Q. Wang, J. Luo and R. Chen, *Adv. Funct. Mater.*, 2020, **30**, 1904815.
12 G. Reichenauer, U. Heinemann and H. P. Ebert, *Colloids Surf., A*, 2007, **300**, 204–210.
13 K. Swimm, G. Reichenauer, S. Vidi and H. P. Ebert, *Int. J. Thermophys.*, 2009, **30**, 1329–1342.
14 C. Bi, G. H. Tang, Z. J. Hu, H. L. Yang and J. N. Li, *Int. J. Heat Mass Transfer*, 2014, **79**, 126–136.
15 N. Hosono, W. Guo, K. Omoto, H. Yamada and S. Kitagawa, *Chem. Lett.*, 2019, **48**, 597–600.
16 J. Tang, J. Sisler, N. Grishkewich and K. C. Tam, *J. Colloid Interface Sci.*, 2017, **494**, 397–409.
17 D. Trache, M. H. Hussin, M. K. M. Haafiz and V. K. Thakur, *Nanoscale*, 2017, **9**, 1763–1786.
18 X. Ren, M. Song, J. Jiang, Z. Yu, Y. Zhang, Y. Zhu, X. Liu, C. Li, H. Oguzlu-Baldelli and F. Jiang, *Adv. Eng. Mater.*, 2022, **24**, 2101534.
19 Z.-G. Jiang, W.-T. Mao, D.-P. Huang, Y. Wang, X.-J. Wang and C.-H. Zhan, *Nanoscale*, 2020, **12**, 10166–10171.
20 K. J. De France, T. Hoare and E. D. Cranston, *Chem. Mater.*, 2017, **29**, 4609–4631.
21 N. Mehra, L. Mu and J. Zhu, *Compos. Sci. Technol.*, 2017, **148**, 97–105.
22 Y. Guo, K. Ruan, X. Shi, X. Yang and J. Gu, *Compos. Sci. Technol.*, 2020, **193**, 108134.
23 J. Yang, C.-R. Han, J.-F. Duan, M.-G. Ma, X.-M. Zhang, F. Xu, R.-C. Sun and X.-M. Xie, *J. Mater. Chem.*, 2012, **22**, 22467–22480.
24 S. Karamikamkar, H. E. Naguib and C. B. Park, *Adv. Colloid Interface Sci.*, 2020, **276**, 102101.
25 Q. Wang, H. Yu, Z. Zhang, Y. Zhao and H. Wang, *J. Colloid Interface Sci.*, 2020, **573**, 62–70.
26 M. A. B. Meador, E. J. Malow, R. Silva, S. Wright, D. Quade, S. L. Vivod, H. Guo, J. Guo and M. Cakmak, *ACS Appl. Mater. Interfaces*, 2012, **4**, 536–544.
27 J. Zeng, Z. Chen, M. Li, Y. Guo, J. Xu, X. Zhao and H. Lu, *Chem. Mater.*, 2022, **34**, 9172–9181.
28 T. Köhnke, T. Elder, H. Theliander and A. J. Ragauskas, *Carbohydr. Polym.*, 2014, **100**, 24–30.
29 J. Lee and Y. Deng, *Soft Matter*, 2011, **7**, 6034–6040.
30 H. Jiang, W. Su, P. T. Mather and T. J. Bunning, *Polymer*, 1999, **40**, 4593–4602.
31 Z. Zheng, Q. Zhou, M. Li and P. Yin, *Chem. Sci.*, 2019, **10**, 7333–7339.
32 C. Fontes-Candia, A. Ström, L. G. Gómez-Mascaraque, A. López-Rubio and M. Martínez-Sanz, *Algal Res.*, 2020, **47**, 101882.
33 H. Wang, R. Song, M. Li, C. Liu, Y. Ke and P. Yin, *Biomacromolecules*, 2022, **23**, 3329–3335.
34 G. Paladini, V. Venuti, L. Almásy, L. Melone, V. Crupi, D. Majolino, N. Pastori, A. Fiorati and C. Punta, *Cellulose*, 2019, **26**, 9005–9019.
35 N. Lavoine and L. Bergström, *J. Mater. Chem. A*, 2017, **5**, 16105–16117.
36 G. Chu, D. Qu, E. Zussman and Y. Xu, *Chem. Mater.*, 2017, **29**, 3980–3988.
37 P. Liu, X. Li, P. Min, X. Chang, C. Shu, Y. Ding and Z.-Z. Yu, *Nano-Micro Lett.*, 2020, **13**, 22.
38 P. Min, X. Li, P. Liu, J. Liu, X.-Q. Jia, X.-P. Li and Z.-Z. Yu, *Adv. Funct. Mater.*, 2021, **31**, 2103703.
39 J. Yang, W. Yang, W. Chen and X. Tao, *Prog. Polym. Sci.*, 2020, **109**, 101289.
40 Y. Cui, H. Gong, Y. Wang, D. Li and H. Bai, *Adv. Mater.*, 2018, **30**, 1706807.
41 X. Qian, L. Song, Y. Bihe, B. Yu, Y. Shi, Y. Hu and R. K. K. Yuen, *Mater. Chem. Phys.*, 2014, **143**, 1243–1252.
42 J. Li, H. Wang and S. Li, *Polym. Degrad. Stab.*, 2019, **164**, 36–45.
43 S. Zhang, Y. Yan, W. Wang, X. Gu, H. Li, J. Li and J. Sun, *Polym. Degrad. Stab.*, 2018, **147**, 142–150.